Structural basis for electromechanical coupling and pore block of human $Ca_v1.4$

Yitong Sun[1,4], Tong Wu[1,4,] Tongtong Wang[1], Huan Wang[1], Jian Huang[2],

Nieng Yan[1,2,3,5], and Zhangqiang Li[1,5]

[1]State Key Laboratory of Membrane Biology, Beijing Advanced Innovation Center for Structural Biology, Tsinghua-Peking Joint Center for Life Sciences, School of Life Sciences, Tsinghua University, Beijing 100084, China

[2]Institute of Bio-Architecture and Bio-Interactions (IBABI), Shenzhen Medical Academy of Research and Translation, Guangming District, Shenzhen 518107, Guangdong Province, China

[3]Institute of Chemical Biology (ICB), Shenzhen Bay Laboratory, Guangming District, Shenzhen 518132, Guangdong Province, China

[4]These authors contributed equally to this work

[5]To whom correspondence should be addressed: N. Yan (nyan@tsinghua.edu.cn) or Z. Li (lizhangq@tsinghua.edu.cn).

Abstract

$Ca_v1.4$ is an L-type calcium channel (LTCC) essential for visual signal transmission. Here, we present cryo-EM structures of human $Ca_v1.4$ alone and in complex with a potent antagonist SR33805, both at resolutions of ~2.9 Å. The fishhook-shaped SR33805 molecule, an indole analogue, penetrates the III-IV fenestration and projects to the central cavity, immediately explaining its mechanism of action. In both structures, VSD_{II} and VSD_{III} display the completely and partially down conformations, respectively, while the other two VSDs are up. The pore domain exhibits a tightly closed conformation. To probe the molecular determinants for the different conformations of VSD_{II} among the four LTCCs, we solved the structure of human $Ca_v1.1$, which features four up VSDs, and generated a $Ca_v1.4$ chimera with VSD_{II} replaced by that from $Ca_v1.1$. The structure of $Ca_v1.4$ chimera shows an up VSD_{II}, suggesting that the conformational determinants may exist within the domain. Consistent with this analysis, substitution of three varied residues resulted in mixed up and down conformations of VSD_{II} in the cryo-EM analysis. Our studies complete the structural gallery of all ten human Ca_v channels, providing a comprehensive framework for comparative analysis of their working and disease mechanisms and for structure-guided drug discovery.

Introduction

Visual signal transmission is a complex, precise, and tightly regulated process that underpins the ability of metazoans to perceive and interpret their surroundings [1,2]. In vertebrates, light is detected by the photoreceptors in the retina, where photons are converted into electrical signals. These signals are subsequently transmitted to the brain through the second-order neurons, such as bipolar and horizontal cells [1-5]. In the retina, the cone photoreceptors enable visual perception during daylight, and the rod photoreceptors are responsible for mediating vision under scotopic conditions. In darkness, photoreceptors maintain a relatively depolarized membrane potential. Activation of the voltage-gated calcium (Ca_v) channels, which are clustered at the ribbon synapses, facilitates the sustained and tonic release of glutamate. Upon exposure to light, the absorption of photons results in membrane hyperpolarization of the photoreceptors, which in turn suppresses the activity of Ca_v channels and reduces glutamate release [6-9].

The primary Ca_v channel in retinal photoreceptors is $Ca_v1.4$, whose function is crucial for the extraordinary sensitivity of the visual system [10,11]. Encoded by the *CACNA1F* gene and classified as an L-type calcium channel (LTCC), $Ca_v1.4$ is characterized by a relatively small unitary conductance, slow inactivation kinetics, and minimal calcium-dependent inactivation (CDI) compared to other LTCCs or high-voltage activated (HVA) subtypes [12-15]. These properties are thought to be critical for sustaining prolonged synaptic transmission in the retina. Mutations in *CACNA1F* are associated with a range of visual disorders, most

notably congenital stationary night blindness type 2 (CSNB2), a non-progressive retinal disorder characterized by impaired night vision and reduced visual acuity [16-18]. $Ca_v1.4$ thereby represents a potential therapeutic target for the treatment of retinal disorders [19].

$Ca_v1.4$ was the last Ca_v channel to be identified, through the Human Genome Project [20]. Consistently, it remained the only mammalian Ca_v subtype whose structure was still at large. Advances in cryo-electron microscopy (cryo-EM) have enabled high-resolution structural determination of eight human Ca_v subtypes, including $Ca_v1.2$-1.3, $Ca_v2.1$-2.3, and $Ca_v3.1$-3.3, since the first structure of a Ca_v channel (rabbit $Ca_v1.1$ isolated from skeletal muscle) was reported ten years ago [21-30]. These structures, determined either in the apo state or in complex with small molecules or peptide toxins, have provided important insights into the molecular basis underlying the physiology, pathophysiology, and pharmacology of Ca_v channels [31,32]. Consistent with the differential physiological and biophysical properties of these channels, their structures are marked with different features.

Whereas Ca_v1 and Ca_v2 subtypes (collectively known as the high-voltage-activated (HVA) Ca_v channels) form complexes with α2δ-1 and β subunits, Ca_v3 channels, which are low-voltage-activated, consist solely of the α1 core subunit [31-35]. Among the HVA Ca_v structures, those of Ca_v2 channels display a closed-state inactivated (CSI) conformation, characterized by a closed pore domain (PD) and one voltage-sensing domain (VSD) in the down conformation [25-27]. In contrast, the core structures of $rCa_v1.1$ and human $Ca_v1.3$

resemble those of the Ca_v3 subfamily, featuring a more relaxed yet still non-conductive PD, with all four VSDs in the up conformation [21,22,24,28-31]. Human $Ca_v1.2$ has been captured in several conformations, among which VSD_{II} in the apo state adopts a down conformation similar to that in Ca_v2 channels, whereas the relaxed PD resembles those of $rCa_v1.1$ and $Ca_v1.3$ [23,31]. It is also noted that unlike the human $Ca_v1.2$, $Ca_v1.3$ and $Ca_v1.4$ channels, which were recombinantly co-expressed with different α2δ and β subunits in HEK293F cells, $rCa_v1.1$ was isolated from rabbit skeletal muscle and, in addition to the α2δ and β subunits, associated with an endogenous γ subunit [21,22]. What determines the conformational differences between $Ca_v1.2$ and $rCa_v1.1$/$Ca_v1.3$ remains unclear, and the structures of human $Ca_v1.4$, as well as human $Ca_v1.1$, are yet to be determined.

Here, we present the cryo-EM structures of human $Ca_v1.1$ and $Ca_v1.4$ in complex with the auxiliary subunits α2δ-1 and β3. Whereas the structure of human $Ca_v1.1$ is nearly identical to that of $rCa_v1.1$, the $Ca_v1.4$ structure reveals a unique conformation, with VSD_{II} in a down conformation and VSD_{III} in a partially down conformation. Structure-guided sequence comparison of $Ca_v1.4$ with other LTCCs identifies the molecular determinants responsible for the distinct conformations of VSD_{II}. Three variable residues in VSD_{II} may underlie the observed structural differences, a finding further corroborated by our structural studies of $Ca_v1.4$ variants. Furthermore, to explore the structural pharmacology of this channel, we determined the structure of $Ca_v1.4$ in complex with a small molecule blocker, SR33805, and revealed the molecular details underlying its mechanism of action (MOA).

Results

The four VSDs of $Ca_v1.4$ exhibit three distinct conformations

Before structural analysis of human $Ca_v1.4$, we validated the channel activity of recombinantly expressed full-length α1 (UniProt: O60840-1) in the presence of the auxiliary subunits α2δ-1 and β3. Whole-cell patch-clamp recordings of the channel complexes transiently expressed in HEK293T yielded the steady-state activation and inactivation $V_{1/2}$ of the voltage-dependent Ba^{2+} currents (I_{Ba}) of -6.58 ± 0.22 mV and 2.72 ± 1.71 mV, respectively (Figure 1a). These electrophysiological data are consistent with the reported biophysical characterization of $Ca_v1.4$ [12,14]. Then we performed cryo-EM analysis of the $Ca_v1.4$ ternary complex following our standard protocol [25]. A 3D EM reconstruction was obtained at an overall resolution of 2.9 Å (Figures 1b, S1, S2, Table S1). Both the α1 and α2δ-1 subunits are well resolved; by contrast, the β3 subunit and its interacting AID (α1-interacting domain) motif are invisible. The molecular basis for the poor resolution of AID and β3 will be discussed in a later session.

When the structure of the α1 subunit of $Ca_v1.4$ is superimposed onto those of other LTCCs (Figure S3a), the root-mean-square deviation (RMSD) is 1.3 Å over 934 Cα atoms for $rCa_v1.1$ (PDB: 5GJV), 1.8 Å over 1003 Cα atoms for $Ca_v1.2$ (PDB: 8WE6), and 1.5 Å over 934 Cα atoms for $Ca_v1.3$ (PDB: 7UHG). VSD_I and VSD_{IV} both adopt the up conformation, consistent with those observed in other LTCCs (Figure S3b). VSD_{II}, similar to

that in the apo $Ca_v1.2$ structure, adopts a down conformation, in which four gating charges (R3, R4, K5, and R6) on S4 are positioned below the occluding Phe on S2 (Figure 1c, *left*). VSD_{III}, in contrast to that in all other LTCC structures, displays a partially down conformation, in which $S4_{III}$ moves toward the intracellular side by approximately one helical turn, compared to the up VSD_{III} in $rCa_v1.1$, $Ca_v1.2$, and $Ca_v1.3$ (Figure 1c, *right*).

With the four VSDs exhibiting three distinct states, the structure of the $Ca_v1.4$ complex represents an additional conformation to the Ca_v structural gallery. Interestingly, the VSD conformations in $Ca_v1.4$, in a sense, resemble those in the engineered $Na_v1.7$ variant, named M11, in which VSD_I is completely down and VSD_{II} is partially down [36].

Distinctive features of the pore domain (PD) in $Ca_v1.4$

Apart from the unique VSD conformations, the PD of $Ca_v1.4$ is tighter than that in the other three LTCCs. As the apo $Ca_v1.2$ structure also shows a down VSD_{II}, we focused on the comparison between these two channels to avoid redundant depiction. When the apo structures of $Ca_v1.4$ and $Ca_v1.2$ are superimposed relative to their PD, VSD_{II} and VSD_{III} in $Ca_v1.4$ rotate around the PD clockwise from those in $Ca_v1.2$ in the intracellular view, with VSD_{II} to a greater degree (Figure 2a). The conformational changes within the VSDs and their domainwise rotations are coupled to the structural shifts of PD via the S4-5 segments, offering important clues to the electromechanical coupling mechanism in Ca_v channels.

The one-helical turn downward movement of $S4_{III}$ from $Ca_v1.2$ to $Ca_v1.4$ results in a shift of $S4\text{-}5_{III}$ toward the PD compared to that in $Ca_v1.2$ (Figure 2b). This seemingly subtle displacement triggers concerted conformational rearrangements of multiple PD segments, similar to what has been observed between $Na_v1.7$-M11 and WT [36]. Specifically, the shift of $S4\text{-}5_{III}$ drives $S6_{III}$ closer to the central axis of the PD to avoid steric hindrance. The ensuing shift of $S6_{III}$ subsequently influences its neighboring helices, $S6_{II}$ and $S6_{IV}$, allowing sufficient space to accommodate rearrangements of PD segments(Figure 2b, *left*).

Of particular note, the movement of $S6_{II}$ pulls the distal portion of $S6_I$ to shift away from the central axis, thus increasing the freedom of the ensuing AID motif. This increased flexibility may account for the invisibility of the AID motif and its bound β3 subunit in the EM map of $Ca_v1.4$ (Figure 2b, *right*).

In addition to the positional displacements of the S6 segments, $S6_I$ and $S6_{III}$ undergo helical rotations when compared pairwise between $Ca_v1.4$ and $Ca_v1.2$ (Figure S4a). These two S6 segments in $Ca_v1.2$ each contain a π-helical turn approximately in the middle of the membrane, but consist entirely of α-helical turns in $Ca_v1.4$; the axial rotation of each helix occurs after Gly359 and Ala1125, respectively (Figure S4).

The transition between α- and π-helical conformations leads to a rearrangement of the gating residues and thus the state of the intracellular gate. For instance, in $Ca_v1.2$, Phe408 and

Phe1189 rotate away from the central axis of the PD, whereas the corresponding residues in $Ca_v1.4$, Phe375 and Phe1140, are both oriented toward the central pore and form a π-π stacking interaction. Together with Leu761 and Phe1444, these interactions seal the intracellular gate of $Ca_v1.4$ (Figure 2c). Thus, transitions between α- and π-helical conformations of S6 directly regulate the gating of Ca_v channels, a mechanism that has also been observed in Na_v channels [36,37]. Furthermore, the conformation of $Ca_v1.4$, which likely represents a CSI state, provides insights into the resting state, which is likely characterized by a tightly closed PD and four VSDs in the "down" conformation [38].

Pore blocking of $Ca_v1.4$ by SR33805

LTCCs represent important drug targets; their antagonists are generally classified into three major groups: dihydropyridines (DHP), benzothiazepines (BTZ), and phenylalkylamines (PAA), all of which have been used clinically for decades [33,34,39-43]. However, several potent blockers do not fall into any of these classes [44]. Among these, SR33805, a synthetic compound structurally related to fantofarone, is classified as a substituted indole [45,46].

Previous studies have shown that SR33805 competitively inhibits fantofarone binding to LTCCs, and allosterically prevents the binding of classical DHP, BTZ, and PAA compounds [45-48]. These characterizations suggest that SR33805 and fantofarone might share a common binding site on LTCCs that deviates from those of the classical antagonists. To

investigate its MOA, we solved the cryo-EM structure of SR33805 bound to $Ca_v1.4$ (Figure S5, Table S1).

In the 2.9 Å cryo-EM map, the density corresponding to the fishhook-shaped molecule of SR33805 is well resolved (Figure 3a). The distinctive contour of the 3,4-dimethoxyphenyl group of SR33805 enables unambiguous fitting of the ligand into the density. SR33805 penetrates the fenestration formed between the PD segments of repeats III and IV, a site defined as F3 (Figure 3b) [32,49,50]. The 3,4-dimethoxyphenyl group of SR33805 resides inside the PD, while the indole group is located outside the PD. SR33805 is primarily coordinated through hydrophobic interactions with residues from repeats III and IV. In addition, Phe1425 in $S6_{IV}$ interacts with the phenoxy linker through π-π stacking (Figure 3c).

In addition to $Ca_v1.4$ residues, two well-resolved linear densities that can be fitted with phosphatidylcholine (PC) participate in the coordination of SR33805 (Figure S6a). The head groups of PC reside in the cavity, and the hydrophobic tails extend outwards from the I-II fenestration. These head groups not only shape the binding pocket, but also provide H-bonds through the phosphoryl group to the amine linker of SR33805 (Figure S6b). Such lipid-facilitated ligand binding has been observed in several drug-bound Ca_v structures, suggesting a conserved paradigm [23,29,51,52].

SR33805, fantofarone, and PAA share a common chemical group of a 3,4-dimethoxyphenyl linked to an amine via an alkyl chain (Figure S6c). The cryo-EM structure of $Ca_v1.1$ in complex with verapamil, a prototypical PAA drug, revealed two distinct binding poses, designated as V1 and V2 [53]. Both poses are located within the central cavity, which is now referred to as site C [32,49,50]. When the structures of verapamil-bound $Ca_v1.1$ and SR33805-bound $Ca_v1.4$ are superimposed, the binding pose of SR33805 partially overlaps with V1, but deviates from V2 (Figure 4, Figure S6c). Moreover, the 3,4-dimethoxyphenyl groups of SR33805 and verapamil in V1 are aligned at nearly identical orientations and positions, whereas their respective alkylamine linkers extend in different directions (Figure 4b). These structural observations, explaining how SR33805 allosterically prevents the binding of classical LTCC antagonists, will aid future optimization and rational design of LTCC blockers.

Human $Ca_v1.1$ and r$Ca_v1.1$ exhibit nearly identical conformations

Next, we attempted to pinpoint the molecular determinant for the distinct conformations among the LTCCs. To exclude the potential impact of the γ subunit on the channel conformation, we also solved the structure of human $Ca_v1.1$ with α2δ-1 and β3, but in the absence of the γ subunit, for a more systematic comparison.

Protein expression, purification, and cryo-EM analysis of the $Ca_v1.1$ ternary complex with α2δ-1 and β3 were carried out using the same procedures as for $Ca_v1.4$. A 3D EM

reconstruction of the $Ca_v1.1$ complex was obtained at an overall resolution of 2.9 Å (Figure S5, Table S1). The $Ca_v1.1$ structure is nearly identical with that of $rCa_v1.1$, with an RMSD of 1.235 Å over 1023 Cα atoms in the α1 subunit; all four VSDs adopt the "up" conformation (Figure S7).

Grafted VSD_{II} from $Ca_v1.1$ to $Ca_v1.4$ remains up

Among the human LTCC structures, VSD_{II} adopts the up conformation in $Ca_v1.1$ and $Ca_v1.3$, and the down conformation in $Ca_v1.2$ and $Ca_v1.4$, despite their high-sequence similarity (Figures 5a, S7c, S8a). To identify the key determinants underlying the distinct VSD_{II} conformations, we started by engineering a channel chimera with grafted VSD_{II}, named $Ca_v1.4$-$VSD_{II}1.1$, in which residues Asn515 - Ser643 of $Ca_v1.4$ were replaced with the corresponding sequence from $Ca_v1.1$ (residues Asn418 - Ser546) (Figure 5a).

A 3D EM reconstruction of $Ca_v1.4$-$VSD_{II}1.1$ was determined at an overall resolution of 3.3 Å (Figures S5, Table S1). VSD_{II} in the chimera adopts an up conformation, similar to that in $Ca_v1.1$ (Figures 5b, c, S8c, d); whereas VSD_{III} is partially up, resembling that in $Ca_v1.4$. These changes suggest that the conformational differences of VSD_{II} between $Ca_v1.4$ and $Ca_v1.1$ should be determined by sequence variations within the domain *per se*. Before we set out to identify the specific loci, we performed a detailed comparison of the up and down state of VSD_{II}.

Accompanying the upward sliding of $S4_{II}$ from $Ca_v1.4$ to the chimera, a segment of the extracellular loop following $S4_{II}$ refolds to one helical turn, and one and a half helical turns on the intracellular terminus are unwound. Meanwhile, VSD_{II} as a domain undergoes a clockwise rotation when viewed from the extracellular side (Figure 5c). These combined structural shifts are reminiscent of what has been observed in VSD_I between its down state in $Na_v1.7$-M11 and up state in the wild type (WT) channel [36], suggesting a conserved electromechanical coupling between Ca_v and Na_v channels.

From the structural comparison of $Na_v1.7$-M11 and WT, a WNΦΦD (Φ represents hydrophobic residues) motif on the S3 segment was discovered to be conserved in all four VSDs of all human Na_v subtypes and play a critical role in gating charge transfer [36]. This motif is also conserved in Ca_v channels, but with slightly varied sequences. In VSD_{II} of LTCCs, the corresponding sequence is $_{593}$FNRFD$_{597}$ (Figure 5a). In the down conformation of $Ca_v1.4$-VSD_{II}, the top R2 forms a hydrogen bond (H bond) with Asn565 (known as An1) on $S2_{II}$, R3 is stabilized by Glu575 (An2) on $S2_{II}$ and Asp597 on $S3_{II}$, and engages in a cation-π interaction with Phe572, R4 is H-bonded with Asn594 and Asp597, and also interacts with Phe593 via a cation-π interaction (Figure 5d, *left*).

In the up VSD_{II} of $Ca_v1.4$-VSD_{II}1.1, the gating charge-coordinating network is reorganized. The upper gating charge residues R2-R4 form multiple H bonds with acidic residues on the extracellular side, whereas K5 is stabilized by Phe572 and Asp597, and K6 is

coordinated by Phe593 and Asn594 (Figure 5d, *right*). Together, these findings underscore the functional significance and evolutionary conservation of the WNΦΦD motif in coordinating gating charges across Na_v and Ca_v channels.

Potential loci that determine the conformational preference of VSD_{II}

We then sought to identify specific residues in VSD_{II} that determined the conformational preferences. We targeted residues that are conserved in $Ca_v1.1$ and $Ca_v1.3$ but vary in $Ca_v1.2$ and $Ca_v1.4$. Two candidate residues stood out from structure-guided sequence analysis. One is an Ile located on $S2_{II}$, Ile466 in $Ca_v1.1$ and Ile557 in $Ca_v1.3$, that is replaced by Thr558 and Tyr563 in $Ca_v1.2$ and $Ca_v1.4$, respectively. The other is a Thr at the beginning of $S4\text{-}5_{II}$, Thr543 in $Ca_v1.1$ and Thr634 in $Ca_v1.3$, which is replaced by Asn635 and Ala640 in $Ca_v1.2$ and $Ca_v1.4$, respectively (Figures 5a, S8d, e). Gly614 on the $S3\text{-}4_{II}$ loop of $Ca_v1.4$ was also considered. Although the corresponding residue in $Ca_v1.1$ is also Gly, it is Glu in $Ca_v1.3$. We speculate that negatively charged residues on the S3-4 loop may increase the electronegativity on the extracellular side to attract the basic GCs, thus favoring an up conformation. In contrast, the corresponding site in $Ca_v1.2$ is occupied by Lys, a positively charged residue that may help stabilize the down conformation of VSD_{II} (Figures 5a).

To test this analysis, we introduced three point mutations, Y563I, G614E, and A640T, to $Ca_v1.4$, and named the mutant $Ca_v1.4$-3M. To assess the conformational state of VSD_{II} in this construct, we determined its cryo-EM structure. Although the overall resolution of the

3D EM reconstruction reached 2.7 Å, VSD_{II} was barely resolved, suggesting increased structural dynamics upon introduction of these mutations (Figures S5, S9a). By applying 3D Variability Analysis (3DVA), 3D classification, and local refinement, two classes of 3D reconstructions (classes I & II) were obtained both at overall resolutions of 2.9 Å; their primary difference occurs in VSD_{II} (Figures S9).

Despite the relatively weak local densities of VSD_{II} in both classes, the positions of GCs on S4 could still be assigned. $S4_{II}$ adopts a down conformation in class I and an up conformation in class II (Figure S9b, c). Therefore VSD_{II} in these two classes exhibits two distinct conformations, respectively reminiscent of that in $Ca_v1.4$ and $Ca_v1.4$-$VSD_{II}1.1$ (Figures 5e, S9b). The structural observations support the three loci within VSD_{II} to contribute to the conformational preferences among different LTCCs.

Discussion

The structural determination of human $Ca_v1.1$ and $Ca_v1.4$ reported here completes the structural atlas of all ten human Ca_v channel subtypes. These high-resolution cryo-EM structures establish a platform to investigate the physiological, pathophysiological, and pharmacological properties of Ca_v channels. Structural determination of all ten Ca_v subtypes represents another starting point for probing several outstanding puzzles. First, the structure-function relationship, including the dynamic and kinetic properties, of any Ca_v channel is yet to be established. Second, the role of lipids in modulating channel function and ligand

binding should be further explored. And most pertinent to human health, the structures have laid the foundation for rational drug optimization and design, especially with the artificial intelligence-enabled tools [54-58].

The available Ca_v structures thus far all represent different forms of inactivated states. The activated and resting states are still at large. Absence of structures for these key states has limited our understanding of their electromechanical coupling mechanism, and prevented the identification of additional drug binding sites. Therefore, any additional conformation to the structural gallery is important.

Despite the high sequence identity among LTCCs, $Ca_v1.4$ exhibits distinctive structural features of a completely down VSD_{II} and a partially down VSD_{III}. Our structure-guided chimeric engineering and mutational characterizations identified three loci, Y563I, G614E, and A640T, to contribute to the conformational dynamics of VSD_{II}. Substitution of the hydrophilic Tyr with a hydrophobic Ile may facilitate the rotation of $S2_{II}$ within the lipid membrane. In addition, the negatively charged Glu may attract and stabilize the positively charged GCs, thereby promoting activation of $S4_{II}$. Upon upward movement of $S4_{II}$, the beginning of $S4\text{-}5_{II}$ helix undergoes partial helical unwinding. In addition, Thr is less favorable for helix formation than Ala, which may further facilitate the upward movement of $S4_{II}$ (Figure 5e). Nevertheless, the precise roles of these residues require further investigation.

In addition to VSD_{II}, VSD_{III} and PD of $Ca_v1.4$ exhibit distinct conformations. The $S4_{III}$ helix shifts downward toward the cytoplasmic side by approximately one helical turn (Figure 1d, *right*). In addition, an unexpected cholesterol-like density is observed near VSD_{III} and $S5_{IV}$ in $Ca_v1.4$. This density is consistently present across $Ca_v1.4$-related structures but is absent in other LTCCs (Figure 6). Since all experimental procedures followed standard protocols, it remains uncertain whether this cholesterol-like density originates from an endogenous sterol or the cholesteryl hemisuccinate Tris salt (CHS) added during protein purification. Nevertheless, this binding pose may be unique to the partially down state of a VSD, hence never observed in any other structures of Ca_v and Na_v channels.

The high-resolution structure of $Ca_v1.4$ allows accurate mapping of 19 disease-associated mutations within the resolved regions (Figure S10a, Table S2), providing a structural framework for understanding the molecular mechanisms underlying CSNB2. For instance, the absence of AID motif in $Ca_v1.4$ structure is due to the conformational shift in $S6_I$, with the transition point located at G369, which is itself a disease-associated mutation site (Figure S10b). This mutation may therefore alter the dynamics of the AID motif, thereby affecting its interaction with the β subunit and associated functions [17,59].

We recently proposed a nomenclature system for ligand binding sites on Ca_v and Na_v channels, which are well-established drug targets [32,49,50]. The accommodation sites at the fenestrations are referred to as site F. However, for some small molecules, such as SR33805,

that penetrate the fenestration, site F cannot fully reflect the binding pose, as the 3,4-dimethoxyphenyl group of SR33805 resides in the central cavity. Thus, site F3C, “C” denoting the central cavity, may provide a more accurate description of the accommodation for SR33805. A more precise nomenclature of the binding sites not only reflects the MOA of the ligands, but also facilitates future drug development.

Apart from what can be gleaned from the available structures, the intracellular segments, including the I-II loop, the II-III loop, and the regions following the carboxyl-terminal domain, remain to be resolved. These regions are implicated in many disease-related loci, as well as physiologically relevant post-translational modifications and protein-protein interactions. Addressing these key questions may require advances in emerging techniques, such as cryo-electron tomography.

Author contributions: N.Y. and Z.L. conceived the project. Z.L., Y.S., T.Wang performed experiments for structural determination. T.Wu performed and analyzed electrophysiological measurements. All authors contributed to data analysis. N.Y. and Z.L. wrote the manuscript.

Acknowledgements: We thank Dr. Xiaomin Li, Dr. Fan Yang, Tao Liu and Dr. Jianlin Lei for technical support during EM image acquisition. We thank the Tsinghua University Branch of China National Center for Protein Sciences (Beijing) for providing the cryo-EM facility support. We thank the computational facility support on the cluster of Bio-Computing Platform (Tsinghua University Branch of China National Center for Protein Sciences Beijing). This work was funded by National Natural Science Foundation of China (Project 32330052 to N.Y., Project 32401004 to Z.L.). N.Y. thanks the Parkland Foundation for the Mindray Endowed Professorship.

Competing interests

The authors declare no competing interests.

References:

1 Penn, R. & Hagins, W. Signal transmission along retinal rods and the origin of the electroretinographic a-wave. *Nature* **223**, 201-204 (1969). https://doi.org/10.1038/223201a0

2 Lagnado, L. & Baylor, D. Signal flow in visual transduction. *Neuron* **8**, 995-1002 (1992). https://doi.org/10.1016/0896-6273(92)90122-t

3 Kaneko, A. & Shimazaki, H. Synaptic transmission from photoreceptors to bipolar and horizontal cells in the carp retina. *Cold Spring Harb Symp Quant Biol* **40**, 537-546 (1976). https://doi.org/10.1101/sqb.1976.040.01.050

4 Stell, W. The structure and relationships of horizontal cells and photoreceptor-bipolar synaptic complexes in goldfish retina. *Am J Anat* **121**, 401-423 (1967). https://doi.org/10.1002/aja.1001210213

5 Frith, P. & Mehta, A. The retina as a window into the brain. *Lancet Neurol* **20**, 892 (2021). https://doi.org/10.1016/S1474-4422(21)00332-X

6 Heidelberger, R., Thoreson, W. & Witkovsky, P. Synaptic transmission at retinal ribbon synapses. *Prog Retin Eye Res* **24**, 682-720 (2005). https://doi.org/10.1016/j.preteyeres.2005.04.002

7 Yau, K. Phototransduction mechanism in retinal rods and cones. The Friedenwald Lecture. *Investigative ophthalmology & visual science* **35**, 9-32 (1994).

8 Nakatani, K. & Yau, K. Calcium and light adaptation in retinal rods and cones. *Nature* **334**, 69-71 (1988). https://doi.org/10.1038/334069a0

9 Kawamura, S. & Tachibanaki, S. Explaining the functional differences of rods versus cones. *Wiley Interdisciplinary Reviews: Membrane Transport and Signaling* **1**, 675-683 (2012).

10 Waldner, D., Bech-Hansen, N. & Stell, W. Channeling Vision: Ca(V)1.4-A Critical Link in Retinal Signal Transmission. *Biomed Res Int* **2018**, 7272630 (2018). https://doi.org/10.1155/2018/7272630

11 Doering, C., Peloquin, J. & McRory, J. The Ca(v)1.4 calcium channel: more than meets the eye. *Channels (Austin)* **1**, 3-10 (2007).

12 Lee, A. *et al.* Characterization of Cav1.4 complexes (alpha11.4, beta2, and alpha2delta4) in HEK293T cells and in the retina. *J Biol Chem* **290**, 1505-1521 (2015). https://doi.org/10.1074/jbc.M114.607465

13 Singh, A. *et al.* C-terminal modulator controls Ca2+-dependent gating of Ca(v)1.4 L-type Ca2+ channels. *Nat Neurosci* **9**, 1108-1116 (2006). https://doi.org/10.1038/nn1751

14 Doering, C., Hamid, J., Simms, B., McRory, J. & Zamponi, G. Cav1.4 encodes a calcium channel with low open probability and unitary conductance. *Biophys J* **89**, 3042-3048 (2005). https://doi.org/10.1529/biophysj.105.067124

15 Baumann, L., Gerstner, A., Zong, X., Biel, M. & Wahl-Schott, C. Functional characterization of the L-type Ca2+ channel Cav1.4alpha1 from mouse retina. *Invest Ophthalmol Vis Sci* **45**, 708-713 (2004). https://doi.org/10.1167/iovs.03-0937

16 Bech-Hansen, N. *et al.* Localization of a gene for incomplete X-linked congenital stationary night blindness to the interval between DXS6849 and DXS8023 in Xp11.23. *Hum Genet* **103**, 124-130 (1998). https://doi.org/10.1007/s004390050794

17 Strom, T. *et al.* An L-type calcium-channel gene mutated in incomplete X-linked congenital stationary night blindness. *Nat Genet* **19**, 260-263 (1998). https://doi.org/10.1038/940

18 Striessnig, J., Bolz, H. & Koschak, A. Channelopathies in Cav1.1, Cav1.3, and Cav1.4 voltage-gated L-type Ca2+ channels. *Pflugers Arch* **460**, 361-374 (2010). https://doi.org/10.1007/s00424-010-0800-x

19 Ganglberger, M. & Koschak, A. Exploring the potential for gene therapy in Cav1.4-related retinal channelopathies. *Channels (Austin)* **19**, 2480089 (2025). https://doi.org/10.1080/19336950.2025.2480089

20 Fisher, S. *et al.* Sequence-based exon prediction around the synaptophysin locus reveals a gene-rich area containing novel genes in human proximal Xp. *Genomics* **45**, 340-347 (1997). https://doi.org/10.1006/geno.1997.4941

21 Wu, J. *et al.* Structure of the voltage-gated calcium channel Cav1.1 complex. *Science* **350**, aad2395 (2015). https://doi.org/10.1126/science.aad2395

22 Wu, J. *et al.* Structure of the voltage-gated calcium channel Ca(v)1.1 at 3.6 A resolution. *Nature* **537**, 191-196 (2016). https://doi.org/10.1038/nature19321

23 Gao, S. *et al.* Structural basis for human Ca(v)1.2 inhibition by multiple drugs and the neurotoxin calciseptine. *Cell* **186**, 5363-5374 e5316 (2023). https://doi.org/10.1016/j.cell.2023.10.007

24 Yao, X., Gao, S. & Yan, N. Structural basis for pore blockade of human voltage-gated calcium channel Ca(v)1.3 by motion sickness drug cinnarizine. *Cell Res* **32**, 946-948 (2022). https://doi.org/10.1038/s41422-022-00663-5

25 Li, Z. *et al.* Structural basis for different omega-agatoxin IVA sensitivities of the P-type and Q-type Ca(v)2.1 channels. *Cell Res* **34**, 455-457 (2024). https://doi.org/10.1038/s41422-024-00940-5

26 Gao, S., Yao, X. & Yan, N. Structure of human Ca(v)2.2 channel blocked by the painkiller ziconotide. *Nature* **596**, 143-147 (2021). https://doi.org/10.1038/s41586-021-03699-6

27 Yao, X. *et al.* Structures of the R-type human Ca(v)2.3 channel reveal conformational crosstalk of the intracellular segments. *Nat Commun* **13**, 7358 (2022). https://doi.org/10.1038/s41467-022-35026-6

28 Zhao, Y. *et al.* Cryo-EM structures of apo and antagonist-bound human Ca(v)3.1. *Nature* **576**, 492-497 (2019). https://doi.org/10.1038/s41586-019-1801-3

29 Huang, J. *et al.* Structural basis for human Ca(v)3.2 inhibition by selective antagonists. *Cell Res* **34**, 440-450 (2024). https://doi.org/10.1038/s41422-024-00959-8

30 He, L. *et al.* Structure, gating, and pharmacology of human Ca(V)3.3 channel. *Nat Commun* **13**, 2084 (2022). https://doi.org/10.1038/s41467-022-29728-0

31 Yao, X., Gao, S. & Yan, N. Structural biology of voltage-gated calcium channels. *Channels (Austin)* **18**, 2290807 (2024). https://doi.org/10.1080/19336950.2023.2290807

32 Huang, J., Pan, X. & Yan, N. Structural biology and molecular pharmacology of voltage-gated ion channels. *Nat Rev Mol Cell Biol* **25**, 904-925 (2024). https://doi.org/10.1038/s41580-024-00763-7

33 Zamponi, G. W., Striessnig, J., Koschak, A. & Dolphin, A. C. The Physiology, Pathology, and Pharmacology of Voltage-Gated Calcium Channels and Their Future Therapeutic Potential. *Pharmacol Rev* **67**, 821-870 (2015). https://doi.org/10.1124/pr.114.009654

34 Dolphin, A. C. A short history of voltage-gated calcium channels. *Br J Pharmacol* **147 Suppl 1**, S56-62 (2006). https://doi.org/10.1038/sj.bjp.0706442

35 Catterall, W. Voltage-gated calcium channels. *Cold Spring Harbor perspectives in biology* **3**, a003947 (2011).

36 Huang, G. *et al.* Unwinding and spiral sliding of S4 and domain rotation of VSD during the electromechanical coupling in Nav1.7. *Proc Natl Acad Sci USA* **119**, e2209164119 (2022). https://doi.org/10.1073/pnas.2209164119

37 Huang, G. *et al.* High-resolution structures of human Nav1.7 reveal gating modulation through alpha-pi helical transition of S6IV. *Cell Rep* **39**, 110735 (2022). https://doi.org/10.1016/j.celrep.2022.110735

38 Li, Z. Q. *et al.* Dissection of the structure-function relationship of Nav channels. *Proceedings of the National Academy of Sciences of the United States of America* **121** (2024). https://doi.org/10.1073/pnas.2322899121

39 Godfraind, T., Miller, R. & Wibo, M. Calcium antagonism and calcium entry blockade. *Pharmacol Rev* **38**, 321-416 (1986).

40 Hockerman, G. H., Peterson, B. Z., Johnson, B. D. & Catterall, W. A. Molecular determinants of drug binding and action on L-type calcium channels. *Annu Rev Pharmacol Toxicol* **37**, 361-396 (1997). https://doi.org/10.1146/annurev.pharmtox.37.1.361

41 Zamponi, G. W. Targeting voltage-gated calcium channels in neurological and psychiatric diseases. *Nat Rev Drug Discov* **15**, 19-34 (2016). https://doi.org/10.1038/nrd.2015.5

42 Weir, M. Diltiazem: ten years of clinical experience in the treatment of hypertension. *J Clin Pharmacol* **35**, 220-232 (1995). https://doi.org/10.1002/j.1552-4604.1995.tb04051.x

43 Triggle, D. Calcium channel antagonists: clinical uses--past, present and future. *Biochem Pharmacol* **74**, 1-9 (2007). https://doi.org/10.1016/j.bcp.2007.01.016

44 Rampe, D. & Triggle, D. J. New ligands for L-type Ca2+ channels. *Trends Pharmacol Sci* **11**, 112-115 (1990). https://doi.org/10.1016/0165-6147(90)90196-f

45 Romey, G., Bois, P. & Lazdunski, M. Effects of two chemically related new Ca2+ channel antagonists, SR33557 (fantofarone) and SR33805, on the L-type cardiac channel. *Eur J Pharmacol* **263**, 101-105 (1994). https://doi.org/10.1016/0014-2999(94)90529-0

46 Chatelain, P., Clinet, M., Polster, P., Christophe, B. & Manning, A. S. In vitro characterization of a novel Ca2+ entry blocker: SR 33805. *Eur J Pharmacol* **246**, 181-193 (1993). https://doi.org/10.1016/0922-4106(93)90030-d

47 Chatelain, P., Dewinkeleer, P., Beaufort, P., Meysmans, L. & Clinet, M. Characterization of the binding of [3H]SR 33805 to the slow Ca2+ channel in rat heart sarcolemmal membrane. *Eur J Pharmacol* **267**, 151-160 (1994). https://doi.org/10.1016/0922-4106(94)90166-x

48 Spedding, M., Kenny, B. & Chatelain, P. New drug binding sites in Ca2+ channels. *Trends Pharmacol Sci* **16**, 139-142 (1995). https://doi.org/10.1016/s0165-6147(00)89002-1

49 Wu, Q. *et al.* Structural mapping of Nav1.7 antagonists. *Nat Commun* **14**, 3224 (2023). https://doi.org/10.1038/s41467-023-38942-3

50 Li, Z., Wu, Q. & Yan, N. A structural atlas of druggable sites on Na(v) channels. *Channels (Austin)* **18**, 2287832 (2024). https://doi.org/10.1080/19336950.2023.2287832

51 Gao, S. & Yan, N. Structural Basis of the Modulation of the Voltage-Gated Calcium Ion Channel Ca(v) 1.1 by Dihydropyridine Compounds*. *Angew Chem Int Ed Engl* **60**, 3131-3137 (2021). https://doi.org/10.1002/anie.202011793

52 Yao, X. *et al.* Structural basis for the severe adverse interaction of sofosbuvir and amiodarone on L-type Ca(v) channels. *Cell* **185**, 4801-4810 e4813 (2022). https://doi.org/10.1016/j.cell.2022.10.024

53 Zhao, Y. *et al.* Molecular Basis for Ligand Modulation of a Mammalian Voltage-Gated Ca(2+) Channel. *Cell* **177**, 1495-1506 e1412 (2019). https://doi.org/10.1016/j.cell.2019.04.043

54 Jimenez-Luna, J., Grisoni, F., Weskamp, N. & Schneider, G. Artificial intelligence in drug discovery: recent advances and future perspectives. *Expert Opin Drug Discov* **16**, 949-959 (2021). https://doi.org/10.1080/17460441.2021.1909567

55 Cao, L. *et al.* De novo design of picomolar SARS-CoV-2 miniprotein inhibitors. *Science* **370**, 426-431 (2020). https://doi.org/10.1126/science.abd9909

56 Jia, Y. *et al.* Deep contrastive learning enables genome-wide virtual screening. *Science* **391**, eads9530 (2026). https://doi.org/10.1126/science.ads9530

57 Miller, E. *et al.* Enabling structure-based drug discovery utilizing predicted models. *Cell* **187**, 521-525 (2024). https://doi.org/10.1016/j.cell.2023.12.034

58 Fink, E. *et al.* Structure-based discovery of nonopioid analgesics acting through the alpha(2A)-adrenergic receptor. *Science* **377**, eabn7065 (2022). https://doi.org/10.1126/science.abn7065

59 Maddox, J. *et al.* A dual role for Ca(v)1.4 Ca(2+) channels in the molecular and structural organization of the rod photoreceptor synapse. *Elife* **9** (2020). https://doi.org/10.7554/eLife.62184

60 Pettersen, E. *et al.* UCSF ChimeraX: Structure visualization for researchers, educators, and developers. *Protein Sci* **30**, 70-82 (2021). https://doi.org/10.1002/pro.3943

61 Lei, J. & Frank, J. Automated acquisition of cryo-electron micrographs for single particle reconstruction on an FEI Tecnai electron microscope. *J Struct Biol* **150**, 69-80 (2005). https://doi.org/10.1016/j.jsb.2005.01.002

62 Zheng, S. *et al.* MotionCor2: anisotropic correction of beam-induced motion for improved cryo-electron microscopy. *Nat Methods* **14**, 331-332 (2017). https://doi.org/10.1038/nmeth.4193

63 Punjani, A., Rubinstein, J., Fleet, D. & Brubaker, M. cryoSPARC: algorithms for rapid unsupervised cryo-EM structure determination. *Nat Methods* **14**, 290-296 (2017). https://doi.org/10.1038/nmeth.4169

64 Rosenthal, P. & Henderson, R. Optimal determination of particle orientation, absolute hand, and contrast loss in single-particle electron cryomicroscopy. *J Mol Biol* **333**, 721-745 (2003). https://doi.org/10.1016/j.jmb.2003.07.013

65 Jumper, J. *et al.* Highly accurate protein structure prediction with AlphaFold. *Nature* **596**, 583-589 (2021). https://doi.org/10.1038/s41586-021-03819-2

66 Varadi, M. *et al.* AlphaFold Protein Structure Database: massively expanding the structural coverage of protein-sequence space with high-accuracy models. *Nucleic Acids Res* **50**, D439-D444 (2022). https://doi.org/10.1093/nar/gkab1061

67 Emsley, P. & Cowtan, K. Coot: model-building tools for molecular graphics. *Acta crystallographica section D: biological crystallography* **60**, 2126-2132 (2004).

68 Adams, P. *et al.* PHENIX: a comprehensive Python-based system for macromolecular structure solution. *Acta Crystallographica Section D: Biological Crystallography* **66**, 213-221 (2010).

69 Davis, I., Murray, L., Richardson, J. & Richardson, D. MOLPROBITY: structure validation and all-atom contact analysis for nucleic acids and their complexes. *Nucleic Acids Res* **32**, W615-619 (2004). https://doi.org/10.1093/nar/gkh398

Figures and figure legends

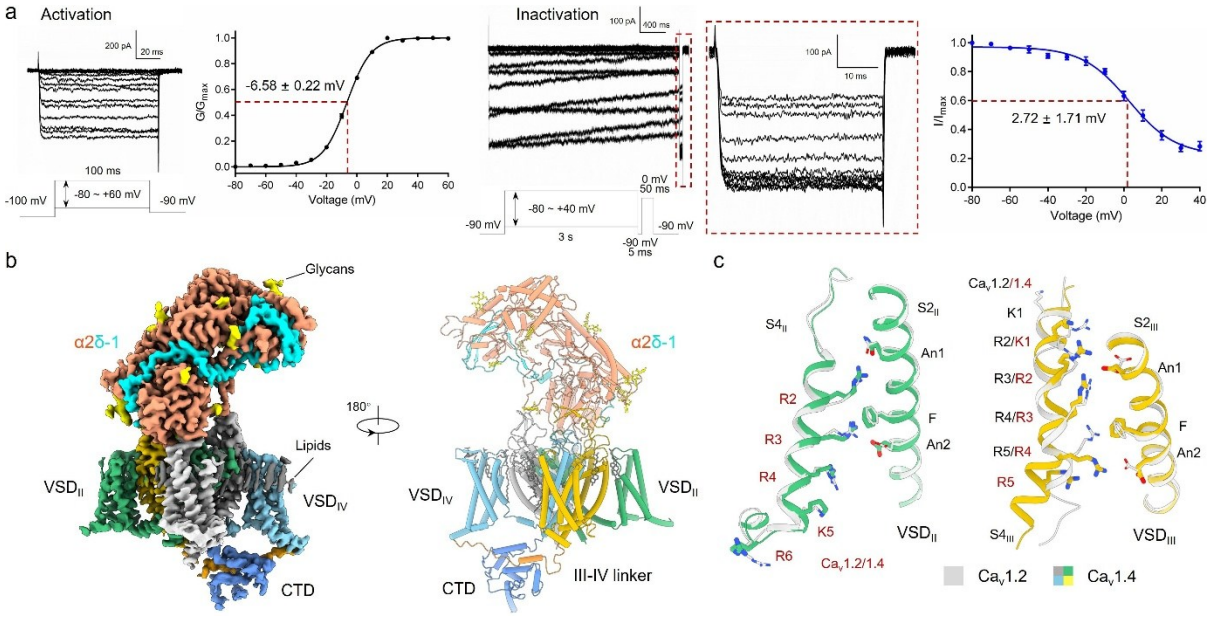

Figure 1 | Cryo-EM structural analysis of human Ca$_v$1.4. **a,** Electrophysiological characterization of recombinantly expressed full-length human Ca$_v$1.4 in complex with the α2δ-1 and β3 subunits. Voltage-dependent activation ($V_{1/2}$ = -6.58 ± 0.22 mV, n = 14) and steady-state inactivation ($V_{1/2}$ = 2.72 ± 1.71 mV, n = 8) analyses, along with the protocols and representative raw traces, are shown. Please refer to Methods and Supplementary Information for experimental details. **b,** Cryo-EM structural determination of the human Ca$_v$1.4 complex. α2, δ1, sugars and lipids are colored salmon, cyan, light yellow and grey, respectively. The transmembrane region of the core subunit α1 is domain-colored, light grey, green, yellow, and light cyan for repeats I-IV, respectively, and the III-IV linker and carboxy-terminal domain (CTD) are colored orange and blue, respectively. No densities corresponding to the α1-interacting domain (AID) or β3 subunit are observed in the cryo-EM map. The same color scheme is applied to the structure of Ca$_v$1.4-apo throughout the manuscript unless otherwise indicated. The cryo-EM map is displayed at a contour level of 6 σ. **c,** The voltage-sensing domains in repeats II and III (VSD$_{II}$ and VSD$_{III}$) of Ca$_v$1.4 exhibit down conformations to different degrees. Structural superimpositions of VSD$_{II}$ and VSD$_{III}$ from Ca$_v$1.4 and Ca$_v$1.2 (PDB: 8WE6, light grey) relative to the charge transfer center are shown. The S1 and S3 segments in both VSDs are omitted for visual clarity. The

conformation of VSD_{II} in $Ca_v1.4$ resembles that of $Ca_v1.2$, adopting a down conformation. $S4_{III}$ is approximately one helical turn lower than that in all other LTCC structures, where VSD_{III} adopts a conformation nearly identical to that in $Ca_v1.2$. All structural figures are prepared in ChimeraX [60].

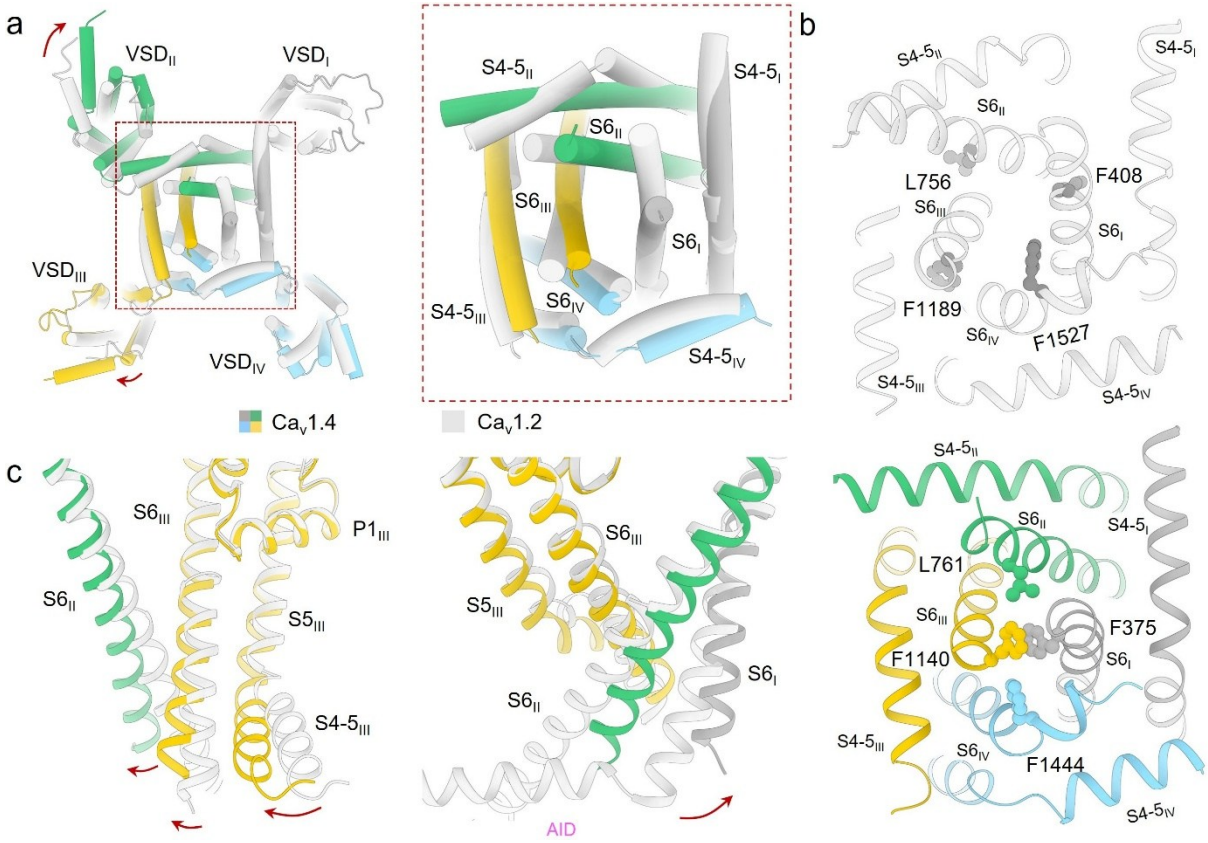

Figure 2 | The non-conductive Ca$_v$1.4 and Ca$_v$1.2 structures exhibit distinct pore conformations. **a,** Coupled conformational changes of the VSDs and pore domain (PD). *Left*: An intracellular view of the superimposed structures of Ca$_v$1.4 and Ca$_v$1.2. The most prominent conformational differences occur in repeats II and III. Red arrows indicate the shifts of the corresponding segments from Ca$_v$1.2 to Ca$_v$1.4. *Right*: enlarged view highlighting conformational differences of the PD. **b,** Further contracted intracellular gate in Ca$_v$1.4. Corresponding gating residues in Ca$_v$1.2 (*top*) and Ca$_v$1.4 (*bottom*) are shown as spheres. **c,** Concerted structural shifts of the S4-5$_{III}$ segment and adjacent PD segments. In Ca$_v$1.4, the S4-5$_{III}$ segment, which immediately follows the partially down VSD$_{III}$, is positioned closer to the central axis of the PD compared with Ca$_v$1.2. The nearby PD segments are pushed towards the center accordingly. Red arrows denote the structural shifts of the related segments from Ca$_v$1.2 to Ca$_v$1.4. AID: The α1-interacting domain, a transverse helical segment that follows S6$_I$.

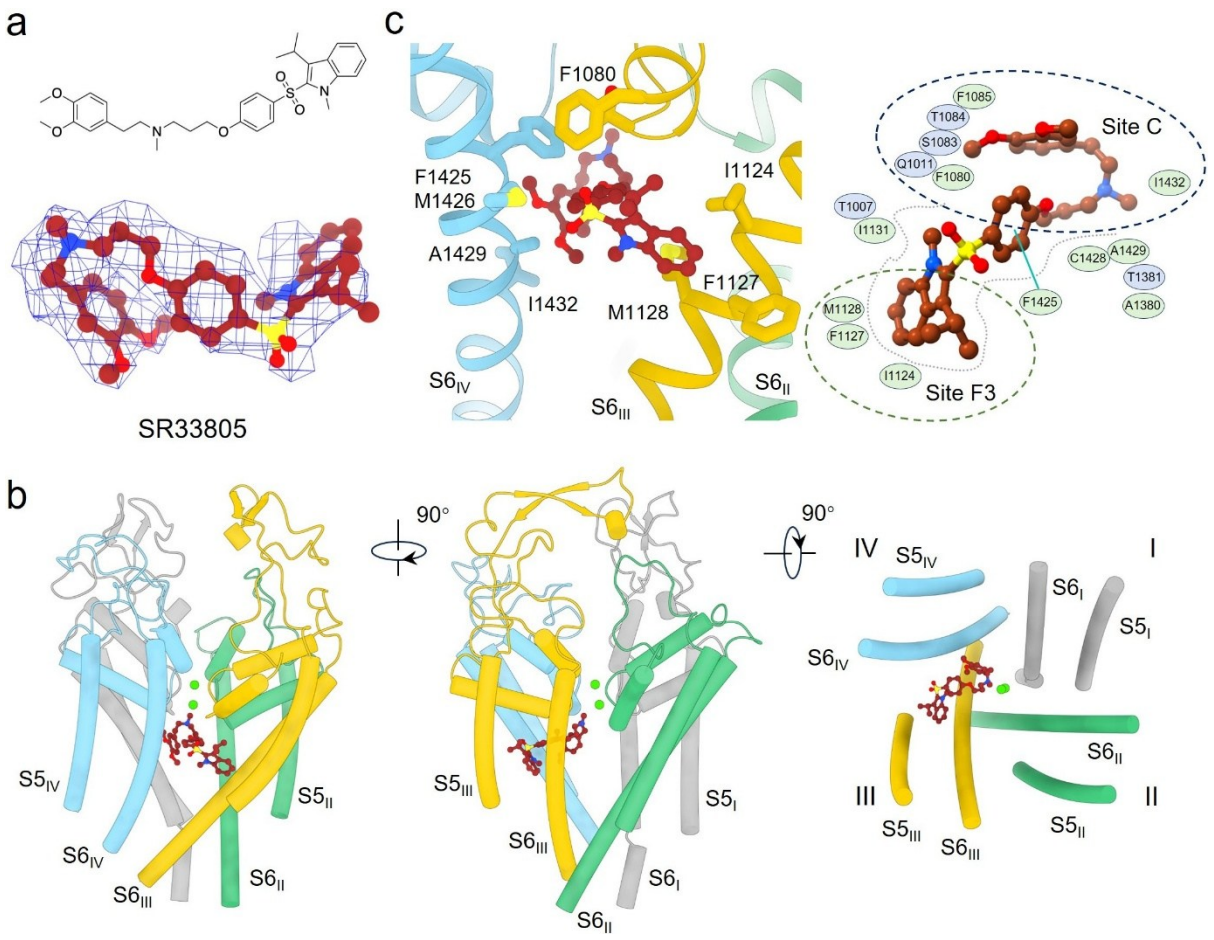

Figure 3 | Molecular basis for pore blockade of $Ca_v1.4$ by SR33805. **a,** Chemical structure of SR33805 and its cryo-EM density. The density map is contoured at a level of 4.5 σ. **b,** SR33805 blocks ion conductance by binding to the III-IV fenestration (site F3) and projecting into the contract cavity (site C). Three views of $Ca_v1.4$ in complex with SR33805 are shown, with the VSDs omitted for visual clarity. SR33805 penetrates into a fenestration formed by repeats III and IV. **c,** Detailed coordination of SR33805. *Left*: SR33805 and surrounding residues are shown as sticks. *Right*: Schematic illustration of residues forming the binding site for SR33805. Residues within a 4-Å cutoff distance to SR33805 are shown. Phe1425 forms a π-π interaction with the phenoxy linker of SR33805.

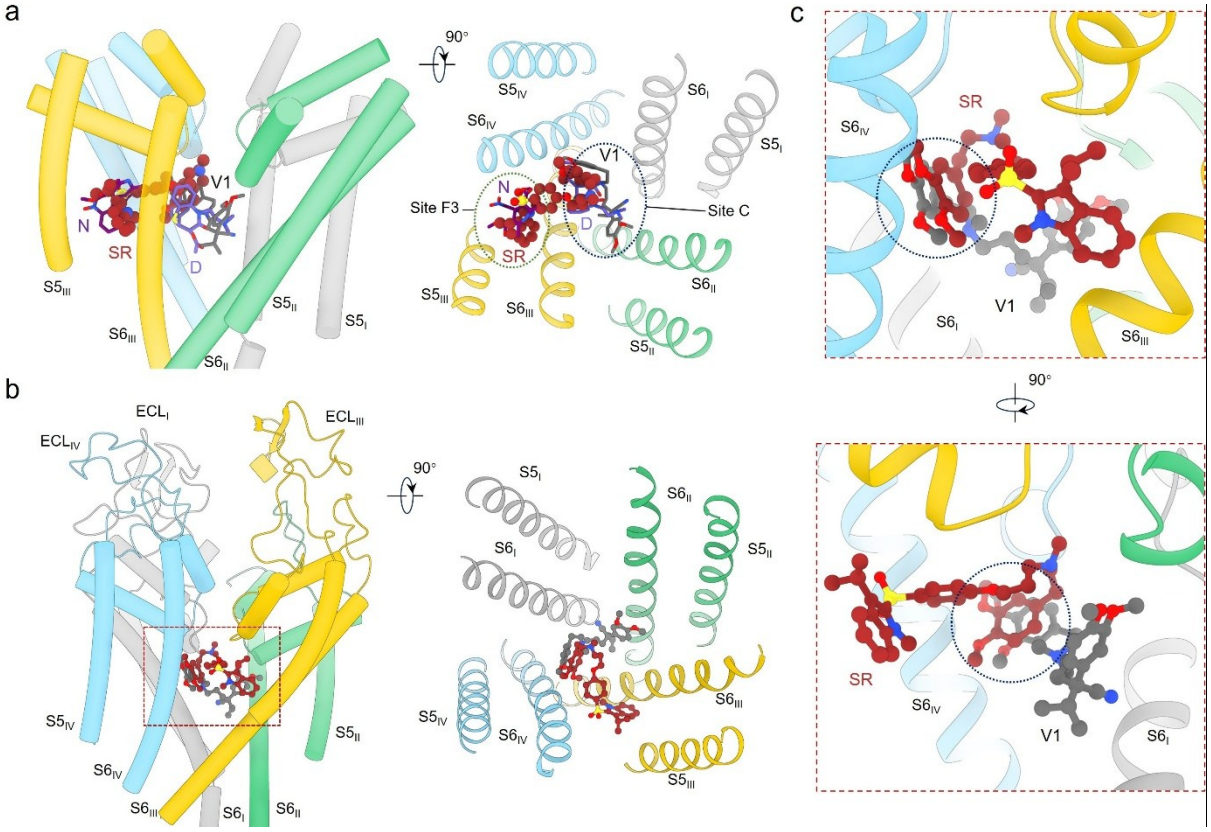

Figure 4 | Structural comparison of SR33805 and representative L-type Ca_v channel antagonists. **a,** Structural comparison of $Ca_v1.4$ bound to SR33805 and previously reported nifedipine, verapamil, and diltiazem. SR33805 is shown in brown spheres and sticks, whereas nifedipine (N, PDB: 6JP5), verapamil (V1, PDB: 6JPA), and diltiazem (D, PDB: 6JPB) are shown as sticks colored purple, grey, and blue, respectively. The corresponding binding sites, site F3 and C, are indicated by dashed circles. For clarity, only the PD of $Ca_v1.4$ is shown. **b,** Structural superimposition of $Ca_v1.4$-SR33805 and $rCa_v1.1$-verapamil (V1, PDB: 6JPA). SR33805 and verapamil (V1) adopt distinct binding poses. Verapamil (dark grey) occupies site C, whereas SR33805 (brown) spans site F3 and site C. **c,** The 3,4-dimethoxyphenyl groups of SR33805 and verapamil (V1 site) are aligned at nearly identical conformations and positions, despite the distinct overall binding poses of the two blockers.

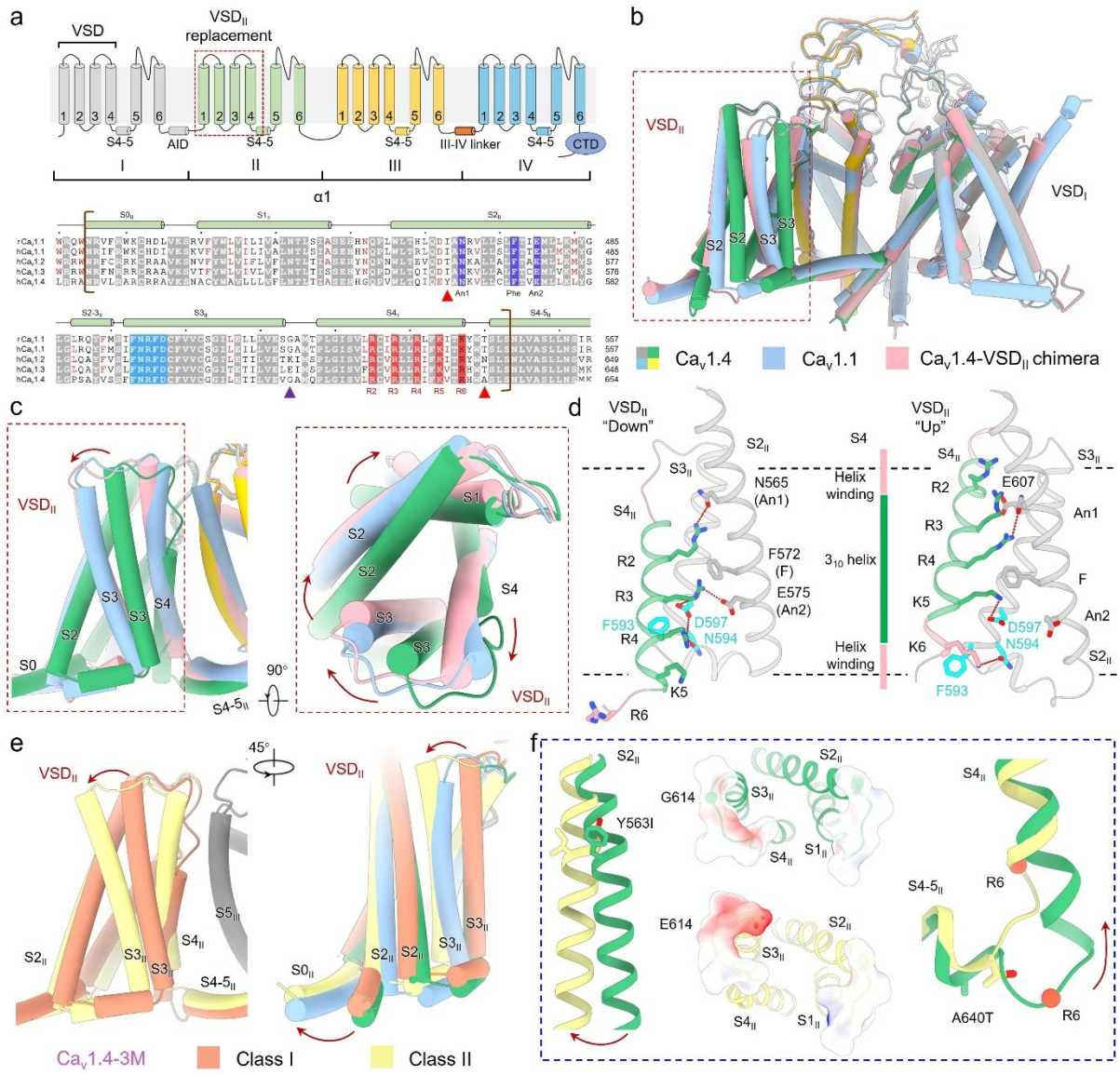

Figure 5 | Structural determinants for the distinct conformations of VSD$_{II}$ among LTCCs. **a,** Engineering of the Ca$_v$1.4-VSD$_{II}$1.1 chimera. The red dashed box on the topological diagram of Ca$_v$1.4 highlights the region replaced by the corresponding segment from human Ca$_v$1.1. Sequence alignment of VSD$_{II}$ in the four human LTCCs and rabbit Ca$_v$1.1 is shown below. The gating charges and the charge transfer center (CTC) residues are shaded red and blue, respectively. The FNRFD motif is shaded cyan, and the key residues that contribute to the distinct VSD$_{II}$ conformations in the LTCCs are indicated with triangles. **b,** The overall structure of the Ca$_v$1.4-VSD$_{II}$1.1 chimera resembles that of Ca$_v$1.1 whose VSD$_{II}$ is up. The structures of human Ca$_v$1.1, Ca$_v$1.4, and the chimera are superimposed relative to their α1 subunit. **c,** Grafted VSD$_{II}$ from human Ca$_v$1.1 retains an up

conformation on the scaffold of $Ca_v1.4$. Accompanying the up-down shift of $S4_{II}$, VSD_{II} displays a domain rotation around the pore domain. Red arrows indicate the rotation of VSD_{II} segments from the down to up conformations. **d,** A conserved FNRFD motif on the cytoplasmic side of $S3_{II}$ stabilizes the gating charge residues in the down conformation of VSD_{II}. The FNRFD motif corresponds to the WNΦΦD motif that stabilizes the down conformation of VSD_I in $Na_v1.7$-M11 [36]. *Left*: Intra-domain coordination of the gating charges in the down state of $Ca_v1.4$-VSD_{II}. The R3 and R4 are stabilized by the FNRFD motif. In addition to the electrostatic interactions, Phe593 contributes a cation-π interaction with R4. *Right*: rearranged coordination of GCs in the up state of VSD_{II} in $Ca_v1.4$-$VSD_{II}1.1$ chimera. The upper three GCs are stabilized by negatively charged residues on the extracellular side, whereas K5 and K6 are coordinated by the FNRFD motif. Dashed lines indicate potential hydrogen bonds. The terminal unwound segments in the down $S4_{II}$ that fold to helical turns accompanying the upward movement of $S4_{II}$ are highlighted pink. **e,** Conformational heterogeneity of VSD_{II} in $Ca_v1.4$-3M (Y563I, G614E, A640T). The triple point mutations were introduced to probe the molecular determinants of the distinct conformations of VSD_{II}. Cryo-EM analysis of $Ca_v1.4$-3M reveals two major conformations, designated Class I (orange) and Class II (yellow). VSD_{II} in classes I and II resembles the down conformation in wild-type $Ca_v1.4$ and the up state in $Ca_v1.1$, respectively. **f,** Molecular basis for the conformational preference determined by the three loci. The loci Tyr563, Gly614, and Ala640 in $Ca_v1.4$-VSD_{II} are replaced by Ile, Glu, and Thr, respectively, in $Ca_v1.3$, whose VSD_{II} adopts an up conformation. G614E may increase the electronegativity on the extracellular side to attract the basic gating charge residues, while Y563L and A640T may affect the interaction between the VSD_{II} segment with the lipid bilayer during the conformational transition.

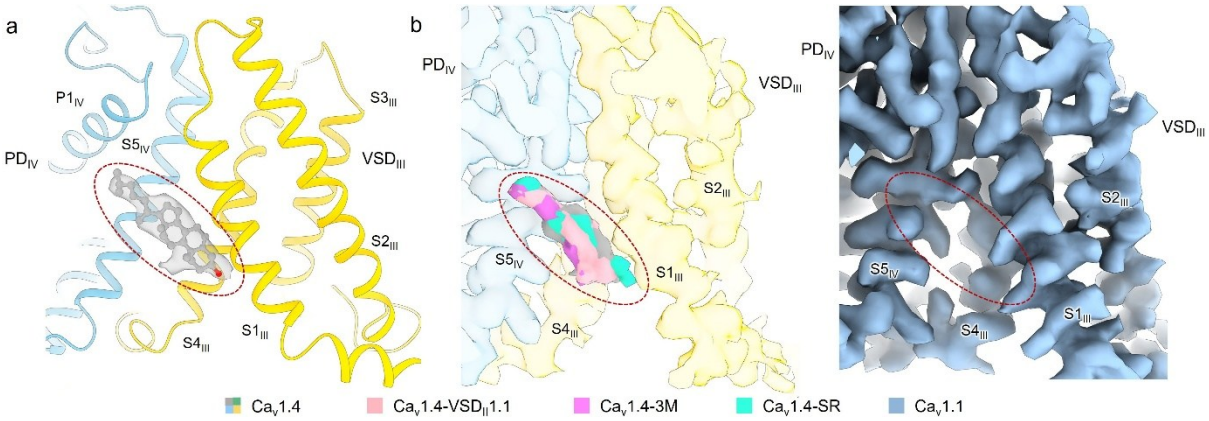

Figure 6 | A unique cholesterol-like density observed in Ca_v1.4. **a,** A sterol-like density is observed in the cleft formed by VSD_{III} and PD_{IV}. This binding pose of a sterol has never been observed in other Ca_v or Na_v structures. **b,** Structural superimposition of Ca_v1.4-related structures reveals a conserved cholesterol-like density in the cleft formed by VSD_{III} and PD_{IV}, but not at the corresponding site in Ca_v1.1, or other LTCCs. The dashed red ovals indicate the sites of the cholesterol-like density. All maps and EM-densities are contoured at 4.5 σ.

Materials and Methods

Transient expression of human Ca_v channel complex in HEK293F cells

Codon-optimized cDNA of *CACNA1F* for full-length human $Ca_v1.4$ α1 isoform 1 (1,977 residues, Uniprot O60840-1), and *CACNA1S* for full-length human $Ca_v1.1$ (1,873 residues, Uniprot Q13698) were synthesized (BGI Geneland Scientific) and subcloned into a pFBDM vector with tandem Twin-Strep and Flag tag at the amino terminus. The auxiliary subunits *CACNA2D1* encoding human α2δ-1 (1,103 residues, Uniprot P54289-1) and *CACNB3* encoding human β3 (484 residues, Uniprot P54284-1) were synthesized and subcloned into the pCAG vector with a carboxy-terminal His_{10} tag. Engineered variants of $Ca_v1.4$, termed $Ca_v1.4$-VSD_{II} chimera and $Ca_v1.4$-3M, were generated using a standard two-step PCR-based strategy. $Ca_v1.4$-VSD_{II} chimera is a chimeric construct in which the VSD_{II} region of $Ca_v1.4$ (residues Asn515-Ser643) was replaced with the corresponding region from $Ca_v1.1$ (Asn418-Ser546). $Ca_v1.4$-3M is a triple mutant carrying substitutions Y563I, G614E, and A640T. Primers were designed using SnapGene and synthesized by Xianghong Biotech. All constructs were verified by Sanger sequencing.

For overexpression of Ca_v channel complex, HEK293F suspension cells were cultured in FreeStyle 293 expression medium (Thermo Fisher Scientific) supplemented with 5% CO_2 at 37 °C. When cell density reached 1.8-2.0 × 10^6 cells per ml, a mixture of expression plasmids with polyethyleneimine (PEI, PolyScience), including 0.9 mg α1, 0.6 mg α2δ-1, 0.5 mg β3, and 4 mg PEI, was added into the cell culture together with 1% (v/v) fetal bovine

serum (FBS, Thermo Fisher Scientific). After transfection for 24 h, the cells were supplemented with 10 mM sodium butyrate and transferred to 30 °C and cultured for an additional 48 h to boost protein expression.

Protein purification of human Ca_V channel complex

Approximately 72 h after transfection, 30 liters of HEK293F cells were harvested by centrifugation at 3,800 rpm for 10 min and resuspended in the lysis buffer containing 25 mM Tris-HCl (pH 8.0), 150 mM NaCl, 2 mM $CaCl_2$ and the protease inhibitor cocktails containing 2 mM phenylmethylsulfonyl fluoride (PMSF), 6.5 μg mL^{-1} aprotinin, 25 μg mL^{-1} leupeptin and 3.5 μg mL^{-1} pepstatin. After sonication and homogenization on ice, the cell membrane was collected by centrifugation at 41,000 rpm for 1 h at 4 °C and resuspended in the lysis buffer supplemented with protease inhibitors. The suspension was then supplemented with detergents to final concentrations of 0.2% (w/v) glyco-diosgenin (GDN, Anatrace), 1% (w/v) n-dodecyl-β-D-maltopyranoside (DDM, Anatrace), and 0.1% (w/v) cholesteryl hemisuccinate Tris salt (CHS, Anatrace). After overnight incubation at 4 °C, the mixture was centrifuged at 13,000 rpm for 50 min at 4 °C, and the supernatant was applied to Strep-Tactin resin (IBA Lifesciences). The resin was rinsed with wash buffer containing 25 mM Tris-HCl (pH 8.0), 150 mM NaCl, 2 mM $CaCl_2$, 0.02% GDN and the protease inhibitor cocktails. After elution with wash buffer plus 2.5 mM D-desthiobiotin (synthesized by GenScript), the eluent was applied to anti-Flag M2 affinity resin (Sigma) and eluted with wash buffer plus 0.2 mg mL^{-1} Flag peptide (synthesized by GenScript). The eluent was

concentrated using a 100-kDa cut-off centricon (Millipore) and further purified through size-exclusion chromatography (Superose 6 10/300 GL, GE Healthcare) pre-equilibrated in the wash buffer. Peak fractions were pooled and concentrated to a final concentration of about 15 mg mL^{-1} for cryo-sample preparation.

For $Ca_v1.4$-drug complex, the concentrated protein solution of wild-type $Ca_v1.4$ was supplemented with SR33805 (MedChemExpress) at a final concentration of 10 μM and the mixture was incubated on ice for 1 h before cryo-EM sample preparation.

Cryo-EM sample preparation and data collection

Aliquots of 4 μl concentrated Ca_v channel complex (including apo-$Ca_v1.4$, apo-$Ca_v1.1$, and $Ca_v1.4$ engineered variants) or $Ca_v1.4$-drug complex were loaded onto the holey carbon grids (Quantifoil Au R1.2/1.3, 300 mesh) glow-discharged for 35 s at medium RF level using a Plasma Cleaner (Harrick). Grids were then blotted for 4 s and plunge-frozen in liquid ethane cooled by liquid nitrogen using a Vitrobot Mark IV (Thermo Fisher Scientific) at 8 °C and 100% humidity. Grid screening was performed on a 200 kV Tecnai Arctica electron microscope (Thermo Fisher Scientific) before data collection. Grids with high quality were transferred to Titan Krios electron microscope (Thermo Fisher Scientific) operated at 300 kV and equipped with spherical aberration (Cs) image corrector for data acquisition. Movie stacks were recorded using a K3 Summit electron detector (Gatan) and a GIF Quantum energy filter (slit width 20 eV, Gatan) in super-resolution counting mode at a nominal

magnification of 64,000×, resulting in a calibrated pixel size of 1.0979 Å. The defocus values varied from -1.3 to -1.8 μm with a step of 0.1 μm. Each micrograph was dose-fractionated into 32 frames with a total dose of about 50 $e^-/Å^2$ and a total exposure time of 2.56 s. AutoEMation was used for fully automated data collection [61].

Image processing

Beam-induced motion of raw movie stacks with 32 frames was corrected with MotionCor2 [62], and dose-weighted micrographs were used for CTF estimation with Patch-CTF estimation in cryoSPARC [63]. Particles were auto-picked using the blob picker. To improve the calculation speed at early stage, particles were extracted and cropped with a binning factor of 2 (Bin2). After 2D classification and *Ab-initio* reconstruction, selected good particles were re-extracted and cropped using a binning factor of 1 (Bin1) for final refinement to obtain high-resolution density maps.

For apo $Ca_v1.4$ and $Ca_v1.1$ complex, 6,763 and 6,065 micrographs were collected, respectively, yielding 4,617,524 and 4,056,147 auto-picked particles in cryoSPARC. After multiple rounds of 2D classification, 737,358 Bin2 particles for $Ca_v1.4$, and 1,276,158 Bin2 particles for $Ca_v1.1$, with different views were selected for *Ab-initio* reconstruction to generate initial reference. Particles corresponding to good reference was then selected and re-extracted in Bin1. The remaining 356,523 ($Ca_v1.4$) and 517,944 ($Ca_v1.1$) particles were subjected to non-uniform refinement and subsequently hetero refinement using the references

generated by *Ab-initio* reconstruction. The good classes after hetero refinement were selected for further non-uniform refinement and local refinement, yielding a density maps at 2.89 Å for apo-$Ca_v1.4$ using 173,010 particles, and 2.90 Å for apo-$Ca_v1.1$ using 161,461 particles.

For $Ca_v1.4$-VSD_{II} chimera, $Ca_v1.4$-3M, and $Ca_v1.4$-SR33805 complex, a total of 3,095, 4,060, and 6,231 micrographs were collected, yielding 1,941,444, 3,059,078 and 4,385,888 auto-picked particles, respectively. Through several rounds of 2D classification, 458,769, 658,352, and 776,839 Bin2 particles were selected. These particles were re-extracted in Bin1 and subjected to hetero refinement, non-uniform refinement, and local refinement using apo-$Ca_v1.4$ as reference. Final reconstructions yielded maps at 3.3 Å for $Ca_v1.4$-VSD_{II} chimera using 203,971 particles, and 2.87 Å for $Ca_v1.4$-SR33805 using 281,113 particles, respectively. The 3D variability analyses (3DVA) and 3D classification were performed on $Ca_v1.4$-3M due to the conformational heterogeneity. Finally, two relatively stable EM maps were obtained with overall resolutions of 2.93 Å (Class I) and 2.87 Å (Class II), using 103,265 and 114,198 particles, respectively.

Resolutions were estimated according to the gold-standard Fourier shell correlation (FSC) 0.143 criterion [64]. Local resolution variations were estimated in cryoSPARC [63].

Model building and refinement

The processes for model building and structural refinement were nearly identical for all structures. In brief, the initial models of human $Ca_v1.4$ and $Ca_v1.1$ α1 subunits were downloaded from the AlphaFold Database with entries AF-O60840-F1 and AF-Q13698-F1, respectively [65,66]. The α2δ-1 subunit was based on the structure of $Ca_v2.2$ (PDB: 7MIY) [26], whereas the β3 subunit is invisible in all structures. All atomic models of $Ca_v1.4$ and $Ca_v1.1$ complexes were first fitted into the corresponding 3D EM maps in ChimeraX [60]. The models were then inspected and manually adjusted in COOT [67]. For engineered variants of $Ca_v1.4$ and $Ca_v1.4$-SR33805 complex, the atomic coordinates of apo-$Ca_v1.4$ were docked into the corresponding maps, and substituted regions or mutated residues were manually adjusted in COOT to match the sequences. SR33805 and additional lipids were manually built into the corresponding densities in COOT.

The final models were refined using PHENIX with secondary structure and geometry restraints in real space [68]. The structures were validated through examination of the Clash scores, MolProbity scores, and statistics of the Ramachandran plots in PHENIX [68,69]. Statistics of the data collection, refinement, and validation can be found in Table S1.

Whole cell electrophysiology of $Ca_v1.4$ complex in HEK293T cells

HEK293T cells were cultured in Dulbecco's Modified Eagle Medium (BI) containing 4.5 mg mL^{-1} glucose and 10% (v/v) fetal bovine serum (BI) at 37 °C with 5% CO_2. After being plated onto glass coverslips and cultured to about 70% confluence, the cells were transiently

co-transfected with the expression plasmids of human $Ca_v1.4$ α1, α2δ-1, β3 subunits together with eGFP-encoding plasmid in the presence of lipofectamine 2000 (Invitrogen). After transfection, cells were cultured at 37 °C for 24 h and then transferred to 30 °C for another 24 h. Then GFP-positive cells were randomly selected for patch-clamp recording. All experiments were performed at room temperature. No further authentication was performed for the commercially available cell line. Mycoplasma contamination was not tested.

The whole-cell Ba^{2+} currents were recorded using an EPC10-USB amplifier with Patchmaster software v2*90.2 (HEKA Elektronik), filtered at 2.9 kHz (low-pass Bessel filter) and sampled at 50 kHz. The glass pipette electrodes (Sutter Instrument) with resistance of 2-4 MΩ were filled with the internal solution containing (in mM) 130 Cesium methanesulfonate, 10 TEA-Cl, 10 EGTA, 5 $MgCl_2$, 5 Na_2ATP, 10 HEPES (pH 7.4 with CsOH and osmolarity of about 310 mosm). The external bath solution composed of (in mM) 95 CsCl, 40 TEA-Cl, 20 $BaCl_2$, 1 $MgCl_2$, 10 D-glucose, 10 HEPES (pH 7.4 with TEA-OH and osmolarity of about 300 mosm).

The voltage dependence of ion current (I-V) was measured by applying voltage pulses to potentials from -80 mV to +60 mV for 100 ms in 10 mV increment from a holding potential of -100 mV. The linear component of leaky currents and capacitive transients were subtracted using the P/4 procedure. Conductance density calculation in the activation

property analysis were fitted with equation, $G= I/(V-V_{rev})$, where V_{rev} (the reversal potential) represents the voltage at which the current is zero.

For voltage dependence of inactivation, cells were held at -90 mV followed by step prepulses from -80 mV to +40 mV for 3 s with an increment of 10 mV. After recover at -90 mV for 5 ms, the currents were recorded at the test pulse of 0 mV for 50 ms. The peak currents under the test pulses were normalized and plotted against the prepulse voltage. Activation and inactivation curves were fitted with a Boltzmann function to obtain $V_{1/2}$ and slope values.

Data were analyzed using Fitmaster 2.90.5 (HEKA Elektronik), Origin (OriginLab) and GraphPad Prism 9.5.1 (GraphPad Software). All data points are presented as mean ± standard error of the mean (SEM) and n is the number of experimental cells from which recordings were obtained.